

ARTICLE OPEN



Impact of the aqueous corrosion induced alteration layer on mechanical properties of pharmaceutical glasses

Qiuju Zheng^{1,4}, Xinlin Ma^{1,4}, Youze Ma¹, Jiaxin Yu², Yuanzheng Yue³ and Hongtu He²

It is known that network modifying ions (such as alkali or alkaline earth ions) make glasses susceptible to aqueous corrosion, resulting in the alteration of their surface layers. However, the effect of the altered layers on the mechanical properties of glasses has not been well understood. In this work we study this effect using the pharmaceutical boroaluminosilicate (BAS) glasses as objects by performing nano- and macroscale mechanical tests. The results show that extending the corrosion time increases the thickness of the alteration layer of the BAS glass. The water-related species in the alteration layer lowers the nanohardness, the reduced modulus, the nanowear resistance and Vickers hardness. The corrosion-induced “silica-like” structure in alteration layer benefits the densification of the subsurface caused by nanoindentation and nanowear, and thereby enhances the fracture toughness of the BAS glass. The correlation between the water content in the alteration layer and the mechanical properties has been revealed. This work is instrumental in the design of the next generation of pharmaceutical glasses with higher toughness.

npj Materials Degradation (2024)8:17 | <https://doi.org/10.1038/s41529-024-00431-3>

INTRODUCTION

The outbreak of the global pandemic (COVID-19) in 2019 has affected billions of human lives, posed critical challenges to the health care system, vaccine manufacturers and pharmaceutical packaging industry¹. The good quality vaccine has been proven to reduce the risk of affecting the COVID-19 and thus save human lives. Nevertheless, without proper packaging and storage of vaccine throughout the entire supply chain, vaccination would be ineffective². Thus, it is extremely important to select proper packing materials of vaccine and pharmaceutical products. Among the primary packaging materials, borosilicate glasses are the most widely used material for packaging vaccines because of their high chemical durability³, and more than 100 billion glass vials are produced and sold globally for various purposes in the past years⁴. However, the emergence of environment-sensitive pharmaceutical products has tightened the requirements on their packaging. Thus, it is of great importance to understand the structure-property relationship of glass, and thereby develop the next generation of pharmaceutical glasses.

Generally, glass vials for pharmaceutical packaging require extremely high chemical durability, i.e., the release of the leachable ions to the vaccine should be avoided⁵. Moreover, to increase the stability and lifetime of vaccine in the glass vials, the surface and subsurface damage of glass during manufacturing process should be avoided, and the contact load during the handing and transportation as well as packaging and storage process should be minimized to prevent potential contact damage on glass surface. Thus, both the mechanical properties and chemical durability of borosilicate pharmaceutical glasses should be greatly improved to increase the stability and lifetime of glass vials. Up to now, numerous studies have shown that the ion-exchange process is an effective approach to strengthen glass vials because such process can help reduce the probability of surface damage⁶. In addition, the surface coating treatment has also been applied to improve the mechanical and chemical

properties because the coating can help lower the coefficient of friction and cosmetic flaws⁷. Those processes require high cost and precise facilities although they enhance the mechanical performances of glass. Recently we have noticed that little attention has been paid to the effect of surface modification by water corrosion on the mechanical properties of pharmaceutical glasses. It is well-known that even without physical contact, water molecules can react with silicate glass surface via hydration, hydrolysis, and/or ion-exchange⁸. According to literature, such chemical reactions of silicate glass surface strongly affect the glass topography⁹, surface chemistry¹⁰, and nanomechanical properties¹¹. In the case of pharmaceutical glass, the water and glass surface interactions are also expected to occur under static conditions¹². Thus, without understanding the effect of water-induced surface corrosion on mechanical properties of pharmaceutical borosilicate glass, it would be impossible to design next generation pharmaceutical glass with superior mechanical properties.

In this study, the evolution of the mechanical properties of a low-boron pharmaceutical boroaluminosilicate (BAS) glass under various corrosion conditions were systematically studied upon nanoindentation, nanoscratch, as well as Vickers indentation tests. To mimic various leaching processes, all glass samples were placed into 50 mL deionized water (unbuffered) in a pressure steam sterilizer for 0 min to 90 min. After the leaching process, atomic force microscopy (AFM), Raman, TOF-SIMS, and sum frequency generation (SFG) spectroscopy were used to characterize the surface roughness, chemical structure, chemical element profile, and hydrogen bonding interactions of adsorbed water species of corroded glass, respectively. The nanoindentation, nanowear, and Vickers indentation tests were performed to reveal the evolution of mechanical properties with altering the glass surface by water corrosion. Based on the experimental results, the evolution mechanism of mechanical properties of borosilicate glasses is discussed.

¹School of Materials Science and Engineering, Qilu University of Technology, Jinan 250353, China. ²Key Laboratory of Testing Technology for Manufacturing Process in Ministry of Education, Southwest University of Science and Technology, Mianyang 621010, China. ³Department of Chemistry and Bioscience, Aalborg University, DK-9220 Aalborg, Denmark. ⁴These authors contributed equally: Qiuju Zheng, Xinlin Ma. email: yy@bio.aau.dk; hehongtu@swust.edu.cn

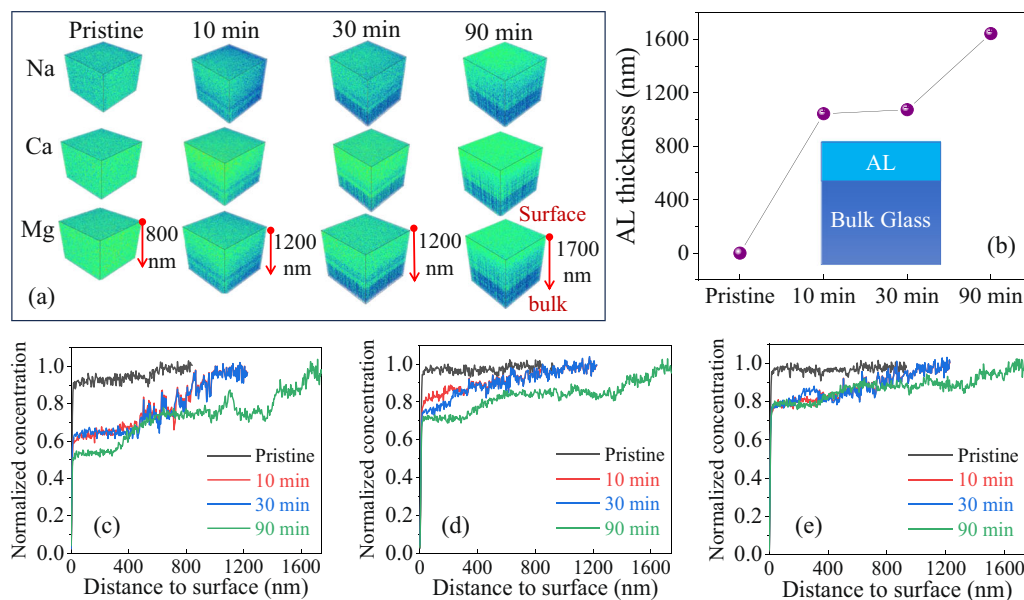


Fig. 1 Surface compositional evolution with extending the corrosion time. **a** ToF-SIMS 3D profile of network modifier distribution in BAS glass surfaces corroded for various time. **b** Alteration layer thickness of BAS glass treated under various corrosion conditions. The concentration of **(c)** Na, **d** Ca, and **e** Mg are normalized to the silicon concentration at the same sputter depth and then normalized by the bulk concentration of each type of ion.

RESULTS AND DISCUSSION

Chemical structure and water content in the alteration layer

When BAS pharmaceutical glasses are treated under accelerated corrosion conditions, the modifying ions in glass structure network such as sodium (Na), Calcium (Ca), and Magnesium (Mg) can be leached out of glass surface, causing the remaining Si-O-Si network change to a “silica-like” or “silica-rich” surface layer, i.e., “alteration layer (AL)”⁹. ToF-SIMS 3D images of network modifying ions distribution in glass surface clearly show that after accelerated corrosion, the concentration of modifying ions at the near-surface region decreases to some extents and it grows to the normal value as the detection depth increases (Fig. 1a). Based on the normalized concentration profile of both network modifiers (Fig. 1c–e) and network formers (Supplementary Fig. 1) of BAS glass as a function of the surface depth, it can be seen that the pristine glass exhibits a slightly depletion of alkali and alkaline earth ions in the range of ~ 500 nm, which is due to the evaporation of alkali and alkaline ions during the sample preparation process.^{13,14} As the corrosion time extends from 0 to 90 min, the alkali ions (Na) and alkaline earth ions (Ca and Mg) are leached out of glass surface, leaving a relatively lower concentration of alkali and alkaline earth ions in the AL (Fig. 1c–e). It is clearly seen that the relative concentration of network modifier ions (Na, Ca, Mg) in the AL decreases with the corrosion time. In the AL, the decrease of Na ions is more pronounced than Ca and Mg ions, owing to the higher mobility and lower ionic radius of Na in BAS glass.^{15,16} Moreover, the relative concentration of network-forming ions (Al and B) in the AL also decreases with extending the corrosion time as a result of the leaching of Al and B out of glass surface (Supplementary Fig. 1).

Following the static corrosion tests conducted for 0, 10, 30, 90 minutes, the pH values of the solution were found to be 7.0, 7.08, 7.11, and 7.19, respectively. The slight increase in pH is attributed to the dissolution of the glass network, wherein mobile ions are leached out of the glass. Moreover, as shown in Fig. 2, all glass network forming and modifying ions are detected through the analysis conducted using the solution based on the inductively coupled plasma-mass spectrometry (ICP-MS). The ion concentration increases with extending the corrosion time,

indicating the dissolution of the etching of the glass network during the static corrosion tests. Using the mass balance of Si species detected in solution compared to the Si initially present in glass, the equivalent thickness of altered glass is calculated¹⁶, as shown in Fig. 2b. It is seen that the equivalent thickness of altered glass increases with corrosion time. Furthermore, the calculated equivalent thickness of altered glass based on boron concentration is notably larger (i.e., ~ 6 times thicker) compared to that determined by silicon. This implies that beyond boron dissolution, an intense boron hydration also occurs, as supported by the depth profile of boron on the glass surface (Supplementary Fig. 1c).

On basis of 3D images and concentration profiles, the corrosion durations of 10, 30, and 90 min give the AL depths of ~ 1.04 μm , ~ 1.07 μm , and ~ 1.6 μm , respectively (Fig. 1b). As the corrosion time increases from 10 to 30 min, the AL thickness is only slightly changed, and this is due to the equilibrium between the dissolution and formation of AL. During this corrosion period, the equivalent thickness of altered glass increases significantly based on the ICP-MS test (Fig. 2b), while the surface RMS roughness of corroded glass increases (Supplementary Fig. 2), implying that the dissolution of AL becomes predominant as the corrosion time increases. However, even though the equivalent thickness of altered glass continues to grow as the corrosion time further increases to 90 min, the AL formation on BAS glass surface becomes predominant, causing the AL thickness increases to ~ 1.64 μm (Fig. 1b).

As the network-modified ions are leached out during the corrosion process, the water molecules from the aqueous solution can diffuse into AL, causing the increase of the hydrous species (such as H_2O , OH^- , and H^+) concentration in the AL. Since the corrosion temperature is relatively high (121 $^\circ\text{C}$), the dominated mechanism of glass corrosion is the hydration of glass network¹⁷. ToF-SIMS 3D images of hydrogen ion concentration in glass surface suggest that the hydration process occurs and the formed hydrous species concentration in the AL increases with the corrosion time (Fig. 3a). The hydrous species concentration can also be detected by Raman spectra (Fig. 3b). It is seen that there is no detectable change in the Si-O-Si links (~ 1050 cm^{-1}), whereas there is a significant increase in OH groups (~ 3100 cm^{-1}) in the subsurface region compared to the pristine glass¹⁸. It is evident

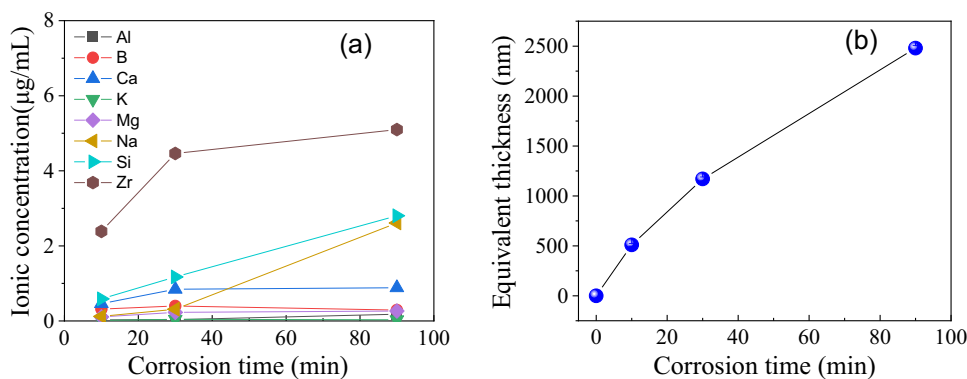


Fig. 2 Corrosion kinetics. **a** Ionic concentration in solution analyzed by ICP-MS and **b** Equivalent thickness of altered glass calculated by silicon concentration under various corrosion conditions.

that the OH group increases with corrosion time (Fig. 3b), suggesting that the glass surface becomes more hydrated with more OH groups in the AL. The total water content in the AL of the glass can be processed based on the Raman spectra¹⁹. It is seen that the total water content in the AL increases with corrosion time (Fig. 3c). Based on the ToF-SIMS and Raman data, the relationship between the total water content and the AL thickness is determined (Fig. 3d). Interestingly, the total water content in the AL increases almost linearly with the AL thickness. To reveal the correlation between the AL and mechanical properties of glass, the mechanical properties of corroded glass are evaluated as a function of water content in the AL in the following sections.

Correlation between the AL and nanoindentation behavior of glass surfaces

The variation in surface chemical structure and water species in surface layer of glass usually lead to the variation in nanomechanical properties of glass.^{20,21} Thus, nanoindentation tests are carried out to measure the variation of BAS glass with varying corrosion conditions. It can be seen in Supplementary Fig. 3a that an extension of corrosion time leads to a decrease of the force that is required for the indenter to penetrate into the same depth of BAS glass surface, suggesting that glass surface becomes softer. Based on the standard Oliver-Pharr model²², the nanohardness and reduced modulus of BAS glass can be calculated from the force-displacement curve in Supplementary Fig. 3a. The reduced modulus, not the elastic modulus, is used here because the exact Poisson's ratio of AL on corroded BAS glass surface is not known¹⁰. As the corrosion time increases from 0 to 90 min, the water content in the AL increases from ~0.03% to ~0.31%, the reduced modulus of BAS glass surface decreases from ~83 to ~75 GPa, and the nanohardness of BAS glass surface decreases from ~7.5 to ~6.4 GPa (Fig. 4a). The pile-up around the nanoindentation of glass surfaces could increase the contact area, and thus the calculated modulus and hardness could be underestimated. However, for a small plastic deformation (i.e., $h_f/h_{max} < 0.7$), the Oliver-Pharr calculation is not significantly affected by the pile-up²³. In fact, the calculated h_f/h_{max} of various BAS glass surface is < 0.7 (Supplementary Fig. 3b), and no obvious pile-up formation around the nanoindentation residual imprint is found (Figs. 4b and c), thus the obtained nanohardness and reduced modulus of BAS glass surfaces by Oliver-Pharr model should be reliable.

Based on the AFM images of the nanoindentation imprint and corresponded cross-section line profile of various BAS glass surfaces, it is found that the nanoindentation imprint becomes wider and deeper with extending the corrosion time (Fig. 4c). As the corrosion time is extended from 0 to 90 min, the indentation depth of BAS glass surface increases from ~104 to ~121 nm, while the corresponded indentation volume increases from $\sim 2.2 \times 10^{-2}$

to $\sim 3.4 \times 10^{-2} \mu\text{m}^3$ (Fig. 4d). The increased indentation depth and volume of various BAS glass surfaces must be related to the structure evolution with varying corrosion times. As the corrosion time extends, the AL thickness in glass surface increases, the remained Si-O-Si network at glass surface region becomes "silica-rich" due to the leaching of modifier ions (such as Na, Ca, and Mg) (Fig. 1). The "silica-rich" structure at glass surfaces exhibited higher nanohardness than pristine glass surface after thermal poling²¹ and SO₂ treatments²⁴ at higher temperature due to the formation of non-hydrous "silica-rich" structure, but it showed a relative lower nanohardness than the pristine glass surface after hydrothermal treatment²⁰ and strong acid treatments²⁵, where substantial H₂O and/or OH species are found in the glass subsurface region. Thus, not only the glass structure, but also the presence of H₂O and/or OH contents in the subsurface region can affect the mechanical properties of the glass. The latter plays a more important role in suppressing the nanohardness and reduced modulus of corroded BAS glass because substantial water-related species are found in the AL of corroded glass surface (Fig. 3).

To reveal the interactions between the hydrous species in the AL and nanomechanical properties of corroded glass surface, the SFG spectra of various glass surfaces is collected. SFG spectroscopy is a second-order non-linear optical technique that has been used extensively to study hydrogen bonding interactions of hydrous species at flat surfaces and interfaces.^{26,27} Through sum frequency generation spectroscopy analysis of corroded glass surface in humid air, it is found that, all BAS glass surfaces show three peaks at ~3130, ~3270, and ~3390 cm⁻¹, and the population of both the lower wavenumbers (~3130 and ~3270 cm⁻¹) and higher wavenumber (~3390 cm⁻¹) increases with the corrosion time (Fig. 5a), indicating that more water molecules impinging from the gas phase can adsorbed on corroded glass surface. Note that the relative concentration of lower wavenumbers to higher wavenumbers increases with corrosion time (Fig. 5b), implying the adsorbed water molecules on corroded glass surface has a stronger hydrogen-bonding interactions with a shorter O-H...O distance²⁰. This suggests that the transition state of the hydrolysis of Si-O-Si network with water under stress condition can be more easily reached or facilitated during nanoindentation process²⁸, resulting in larger indentation depth and volume (Fig. 4d) as well as lower nanohardness and reduced modulus (Fig. 4a) compared to the pristine glass surface. Such decrease in nanohardness and reduced modulus is particularly pronounced for the corrosion time from 30 to 90 min, being consistent with both the pronounced variation in AL thickness and the increase of the hydrous species in the subsurface regions (Figs. 1 and 3).

Not only the surface deformation, but also the subsurface deformation involving densification and shear flow during nanoindentation can be varied if the surface structure of glass is

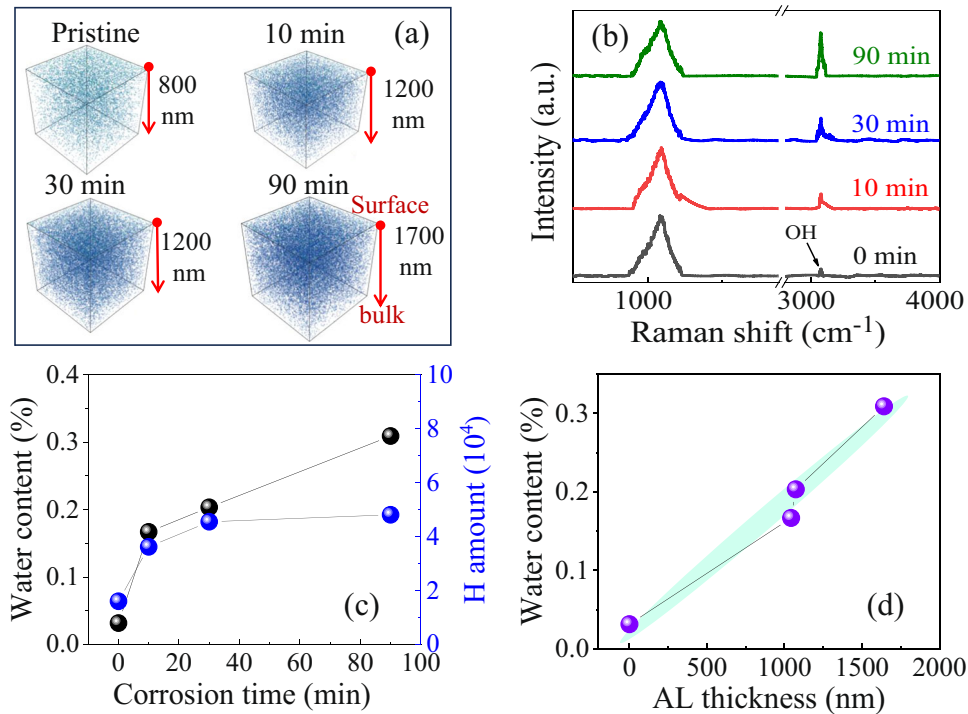


Fig. 3 Change in water content in glass surfaces due to corrosion. **a** ToF-SIMS 3D images of hydrogen ion distributions on the BAS glass surfaces corroded for various durations. **b** Raman spectra of glass surface treated under various corrosion conditions. **c** Relationship between the corrosion time and water content as well hydrogen amount in the AL. **d** Relationship between the AL thickness and the total water content inside the AL under various corrosion conditions.

changed²⁹. It is known that the subsurface densification and shear flow are known as competing processes, and the subsurface densification is a non-volume conservative process, while the shear flow is a volume conservative process³⁰. To verify the variation of subsurface deformation of corroded glass upon indentation tests, all the nanoindentation tracks are annealed for 2 hours and then in-situ re-imaged again with AFM to compare the topography evolution (Fig. 4b, c), based on the methods proposed by Yoshida et al.³¹. The densification volume (V_d) and plastic flow volume (V_p) during nanoindentation process can be also be calculated³¹. As the corrosion time increases from 0 to 90 min, the V_d increases from $\sim 1.3 \times 10^{-2}$ to $\sim 2.4 \times 10^{-2} \mu\text{m}^3$, while the V_p decreases from $\sim 0.98 \times 10^{-2}$ to $\sim 0.89 \times 10^{-2} \mu\text{m}^3$ (Fig. 4e). The recovery ratio (V_R), estimated as the ratio between the V_d and V_i ,⁴⁴ increases from $\sim 60\%$ to $\sim 73\%$ as the corrosion time increases from 0 to 90 min (Fig. 4f). These findings indicate that the densification ratio (or recovery ratio) of BAS glass increases with extending the corrosion time.

Figure 4 shows that both the surface and subsurface damage volumes of the corroded BAS glass increase with extending the corrosion time. This is because the nanoindentation tests are performed at the same penetration depth and the nanohardness of corroded glass surfaces decreases with extending the corrosion time, thus more mechanical energy can be transferred into subsurface region, causing more subsurface deformation of corroded glass. On the other hand, extending the corrosion time leads to an increase of the AL thickness (Fig. 1). Since the AL is more “silica-rich” due to the leaching of modifier ions (such as Na, Ca, Mg) (Figs. 1 and 3), and the pure silica glass is known as the highest propensity to be densified upon the compression by nanoindentation tests³², thus “silica-rich” structure in AL could be responsible for the increase in V_d and V_R of corroded BAS glass surface (Fig. 4e, f).

Correlation between the AL and nanowear behavior of glass surfaces

Not only indentation tests from the surface normal direction, the scratch and/or reciprocating scratch (wear) tests from the tangential directions can also reveal the actual physical contact behavior during the practical application of the glass. To understand the nanowear behavior of corroded BAS glass, the cross-section line profiles of nanowear on BAS glasses, which are subjected to the corrosion for 0 to 90 min, are compared in Fig. 6a. As the corrosion time increases from 0 to 90 min, the nanowear volume increases from $\sim 5.2 \times 10^{-2}$ to $\sim 11.3 \times 10^{-2} \mu\text{m}^3$, while the nanowear depth increases from ~ 9.8 to $\sim 22.6 \text{ nm}$ (Fig. 6d). Interestingly, the nanowear depth and volume follow almost a linear relationship with the water content in the AL, which aligns the facilitated hydrolysis of Si-O-Si network with water under shear stress (Figs. 4 and 5). In addition, the pile-up appears on the periphery of the nanowear mark, and this must be due to the facilitated plastic flow of glass material during the nanowear process.

To explore the subsurface deformation mechanism of corroded BAS glass upon nanowear tests, the AFM images of residual imprints on various glass surfaces are made before and after annealing treatments, and the cross-section line profile of the nanowear mark before and after annealing of BAS glass are compared in Fig. 6c, and the V_p and V_d values are displayed in Fig. 6d. As the corrosion time increases from 0 to 90 min, the V_d increases from $\sim 3.7 \times 10^{-12}$ to $\sim 9.4 \times 10^{-12} \text{ mm}^3$, while the V_p decreases from $\sim 1.8 \times 10^{-12}$ to $\sim 1.5 \times 10^{-12} \text{ mm}^3$. Furthermore, the V_R increases from $\sim 70\%$ to $\sim 83\%$ as the corrosion time increases from 0 to 90 min (Fig. 6e). The increase of V_R with increasing the corrosion time implies that larger subsurface densification volume of glass is caused by the increased AL thickness.

The overall trends in V_p , V_d , and V_R of corroded BAS glass with water content by nanowear tests are consistent with

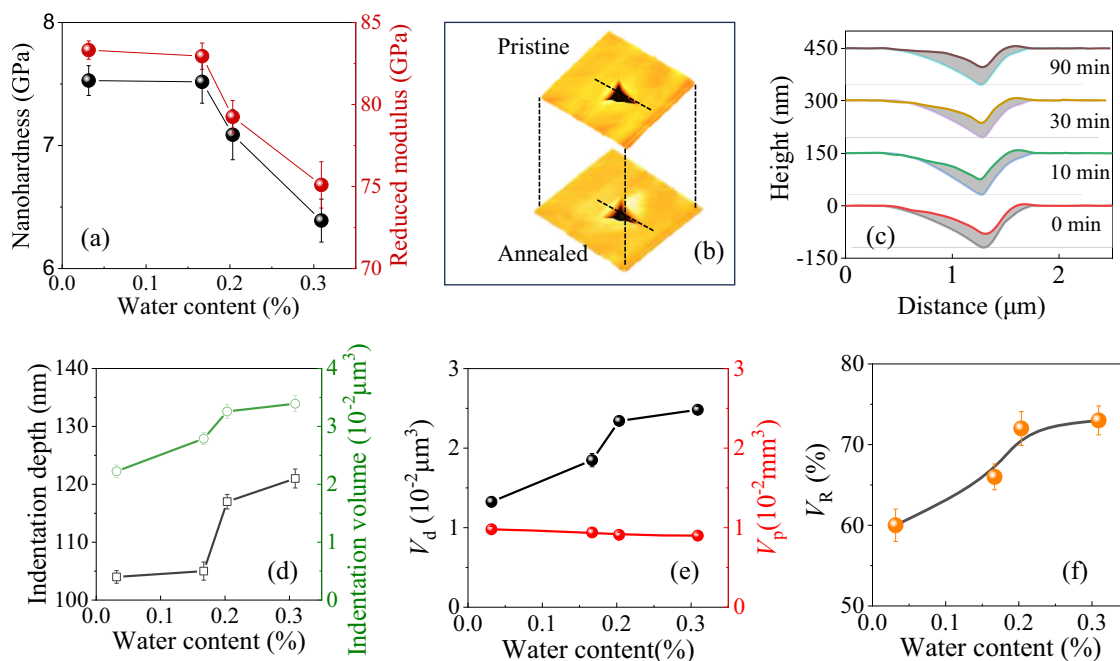


Fig. 4 Mechanical response of glass surface to corrosion time. **a** Nanohardness and reduced modulus of BAS glass surface as a function of water content in the AL. The error bars are based on the standard deviation of 18 measurements for each sample. **b** AFM image and **c** cross-section line profile of residual nanoindentation imprint as well as the corresponding annealed nanoindentation imprint. **d** Indentation depth and volume of residual imprints obtained from **(b)** as a function of water content in the AL. **e** Volumes of plastic flow (V_p) and densification (V_d), **f** Volume recovery ratio (V_R) of corroded BAS glass surface as a function of water content in the AL. The error bars in Figs. 4d–f are based on the standard deviation of 8 measurements for each sample.

nanoindentation tests (Fig. 6), even though the penetration depth of the tip into glass substrate are much lower (<30 nm) during the nanowear tests. The V_R of nanowear mark (Fig. 6e) is higher than that of nanoindentation tests (Fig. 4e), and this could be due to the much smaller depth (<30 nm) of nanowear compared to that of nanoindentation (<130 nm). In the near-surface region, the leaching of alkali and alkaline-earth ions out of glass surface will take place more readily as the depth is lower (Figs. 1 and 3), causing more “silica-rich” structure accompanied with substantial water-related species in the near-surface region. Thus, the mechanochemical reactions of the AL in corroded glass surface with applied stress are more feasible as the penetration depth is lower. This can also explain the wear depth and volume increase by $\sim 130\%$ and $\sim 120\%$ by nanowear tests, respectively (Fig. 6d), and the increase of the residual indentation depth and volume only by $\sim 16\%$ and $\sim 52\%$ by nanoindentation tests, respectively (Fig. 4d).

Correlation between the AL and macroscale mechanical properties of glass surface

Raman and ToF-SIMS measurement show the chemical structure of AL in BAS glass surface become “silica-rich” in the Si-O-Si network after water corrosion, and the hydrous species in AL increases with corrosion time (Figs. 1 and 3). Nanoindentation and nanowear measurements show the nanomechanical properties of BAS glass surface is suppressed, but the subsurface densification is facilitated to some extent by water corrosion (Figs. 4 and 6). These surface layers with modified chemical structures and nanomechanical properties affect the mechanical response of the bulk glasses at the macroscale, which is of critical importance for the stability and lifetime of pharmaceutical products. Thus, the Vickers indentation tests are carried out to reveal the evolution of Vickers hardness of BAS glasses with varying the corrosion conditions, as shown in Fig. 7a. As the corrosion time increases from 0 to 90 min, the Vickers hardness of BAS glass decreases from ~ 6.5 to ~ 5.8 GPa,

and this is consistent with the changing trends of nanohardness (Fig. 4a). Generally, the Vickers hardness of glass surfaces is varied with the structure density in the test regions, even though the probed depth is $\sim 7\mu\text{m}^{33}$. As the corrosion time extends, the network modifying ions are leached out of the glass surface, thereby causing the density decrease of the remaining surface layer, and hence the decrease of the Vickers hardness of corroded glass surface²¹. Moreover, extending the corrosion time leads to an increase of water-related species in the subsurface region (Figs. 1 and 3) and this may facilitate the hydrolysis of glass network during Vickers indentation, leading to the more damaged surface area and thus lower Vickers hardness (Fig. 7a).

In addition to the Vickers hardness, the indentation fracture toughness (K_{IC}) can also be a good indicator for quantifying the resistance to surface defect formation for practical engineering applications. As the corrosion time extends from 0 to 90 min, the K_{IC} of BAS glass surfaces increases from 0.70 to 0.78 $\text{MPa}\cdot\text{m}^{1/2}$ (Fig. 7b). This implies that after corrosion, BAS glass surface becomes more resist to the growth of radial cracks upon Vickers indentation tests, even though the surface hardness decreases (Figs. 4a and 7a). There are two reasons which could be responsible for this. On one hand, the chemical structure of BAS glass surface becomes “silica-rich” after corrosion, as revealed by ToF-SIMS analyses (Figs. 1 and 3). This AL has higher propensity to be densified compared to the pristine glass surface (Figs. 4e and 6e), even though the AL thickness is $<2\mu\text{m}$, which is smaller than the penetration depth of the indenter tip into glass surface ($\sim 7\mu\text{m}$). The subsurface densification is often considered to reduce residual stress around the Vickers indentation impacted area, and thus the glass that undergoes a larger densification shows higher crack resistance and higher K_{IC} ³⁴. On the other hand, as the corrosion-induced AL has propensity to be densified upon the Vickers indentation, the more easily densified surface region can hinder transport of water molecules from the environment to the subsurface crack tip, suppressing the growth of radial cracks under the same Vickers indentation conditions compared to the

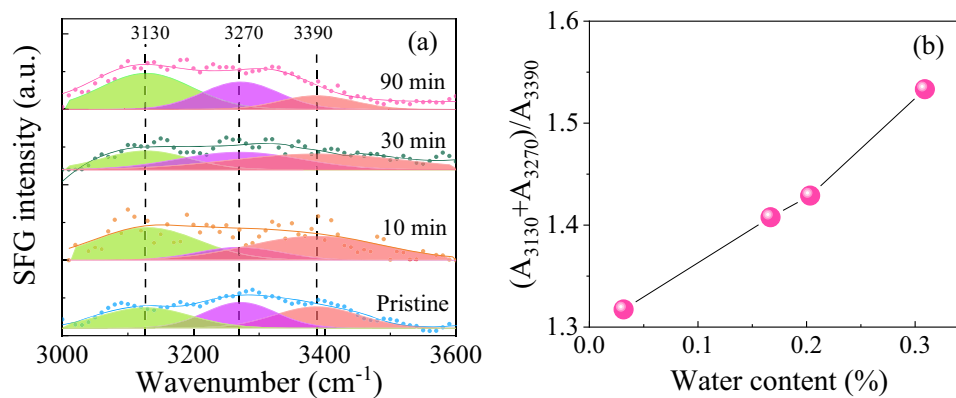


Fig. 5 Sum frequency generation vibration spectroscopy on the corroded glass surface. **a** SFG spectra of glass surfaces under various corrosion conditions, **b** Oscillator strength ratio of the sum of $\sim 3130\text{ cm}^{-1}$ band (A_{3130}) and $\sim 3270\text{ cm}^{-1}$ band (A_{3270}) with the $\sim 3390\text{ cm}^{-1}$ band (A_{3390}) as a function of water content in the AL. The error bar in Fig. 5b is based on the standard deviation of 4 measurements for each sample.

pristine glass surface³⁵. As a result, the corroded BAS glass surface exhibits an increased K_{IC} value (Fig. 7b).

Recently, it is reported that after sodium ions are leached out of the soda-lime-silica glass surface by strong acid treatment, the structure of the leached glass becomes more “silica-like”. Consequently, the average Si-BO bond length decreases while the average Si-O-Si bond angle increases³⁶. Such a structural change at atomic scale can facilitate the subsurface densification under the same loading conditions, and this is why both the subsurface densification and the indentation fracture toughness are enhanced by thermal polishing²¹, SO_2 treatments²⁴, hydrothermal treatment²⁰, and strong acid treatments³⁵. In the case of BAS glass, as boron, alkali, and alkaline-earth ions are leached out of the glass surface (Fig. 1), the Si-O-Si structure of AL also becomes “silica-like”. Therefore, the relaxed structure of AL should show a decrease in the average Si-BO bond length and an increase in the average Si-O-Si bond angle, thereby facilitating the subsurface densification upon indentation and wear tests (Figs. 4d and 6d). As a result, the indentation fracture toughness of BAS glass is increased, and it further increases with the AL thickness (Fig. 7b).

Numerous investigations have demonstrated that the qualitative evolution of the mechanical properties of glass under various surface treatments. For instance, upon the SO_2 treatment in high temperature²⁴, the alteration surface layer of soda lime silica glass has non-hydrated “silica-like” structure, and hence a slightly higher hardness than the pristine glass surface. In contrast, upon strong acid³⁵ or hydrothermal treatment²⁰, the AL of the soda-lime-silica glass surface exhibits the hydrated “silica-like” structure, and therefore it is slightly softer than the pristine glass surface. Nevertheless, the quantitative relationship between the aqueous corrosion-induced AL and the mechanical properties have never been established to date, to the best of our knowledge. In this study, the direct link between the AL and mechanical properties have been revealed for the first time. As the corrosion time increases, the AL thickness and the water content in the AL gradually increase, which could be responsible for the almost linear decrease in a decrease in nanohardness (Fig. 4a), reduced modulus (Fig. 4a), nanowear resistance (Fig. 6d), and Vickers hardness (Fig. 7a) with extending the corrosion time. Thus, upon leaching under various conditions, the generated hydrous species in AL play a critical role in reducing the hardness and modulus measured by nanoindentation tests. On the other hand, as the corrosion time increases, the subsurface densification volume increases almost linear with the AL thickness or the water content in the AL, no matter whether the applied load is from the surface normal direction (indentation tests, Fig. 4e) or from tangential direction (nanowear tests, Fig. 6e), thus it can be stated that the

presence of “silica-like” glass network in the AL plays a critical role in enhancing the fracture toughness of silicate and BAS glass surface.

In summary, the direct connection between the aqueous corrosion-induced AL and the mechanical properties of pharmaceutical BAS glasses has been revealed in this study. An extension of the corrosion time can cause the increase of the AL thickness, and the hydration of structural network. The presence of water-related species in the AL plays a critical role in lowering the nanohardness, the reduced modulus, the nanowear resistance, and the Vickers hardness of the corroded BAS glass. The corrosion-induced “silica-like” structure in AL benefits the densification of the subsurface upon nanoindentation and nanowear tests, and thereby enhances the fracture toughness of the corroded BAS glass. This work is of importance for improving the mechanical properties of glasses and extending their service lifetime.

METHODS

The chemical composition of the glass studied in the present study was $68\text{SiO}_2\text{-}2.2\text{Al}_2\text{O}_3\text{-}2.8\text{B}_2\text{O}_3\text{-}11.6\text{Na}_2\text{O}\text{-}6.7\text{CaO}\text{-}8.6\text{MgO}$ (mol%) according to the X-ray fluorescence analysis. The glass was prepared through conventional melt-quenching method, employing analytical reagent-grade chemicals: SiO_2 , Al_2O_3 , H_3BO_3 , Na_2CO_3 , CaCO_3 , and $(\text{MgCO}_3)_4 \cdot \text{Mg}(\text{OH})_2 \cdot 5\text{H}_2\text{O}$, each having a purity exceeding 99.5%³⁷. 0.1 mol% SnO_2 was added as a fining agent. The raw materials were thoroughly mixed, melted in air in an alumina crucible at $1600\text{ }^\circ\text{C}$ for 2 hours. The melt was first initially poured into water, after which the resultant glass fragments were gathered, dried, and subsequently remelted for 2 h. Finally, the melt was cast onto a copper plate in air and then the obtained glass was annealed for 2 h at the glass transition temperature.^{38,39} The bulk glass samples were cut to a size of $10\text{ mm} \times 10\text{ mm} \times 5\text{ mm}$, where the six faces of glass sample were coarse-polished using 600-, 1500-, 3000-, and 6000-grit SiC papers and fine polished with $1\text{ }\mu\text{m}$ and 80 nm diamond suspensions. Prior to static corrosion tests, the samples were cleaned firstly with distilled water and then with acetone under ultrasonication, and subsequently dried in an oven for 2 hours⁴⁰. For the static corrosion tests, the glass samples were placed into 50 mL deionized water (unbuffered) in a pressure steam sterilizer. The corrosion temperature was set to be $121\text{ }^\circ\text{C}$, while the corrosion time was set to be 10, 30, and 90 min, respectively. The specific static corrosion condition was selected based on the protocol for delamination stress testing of pharmaceutical glasses,^{41,42} although it is slightly different from the standard testing protocol for glass dissolution and leaching tests.^{43,44}

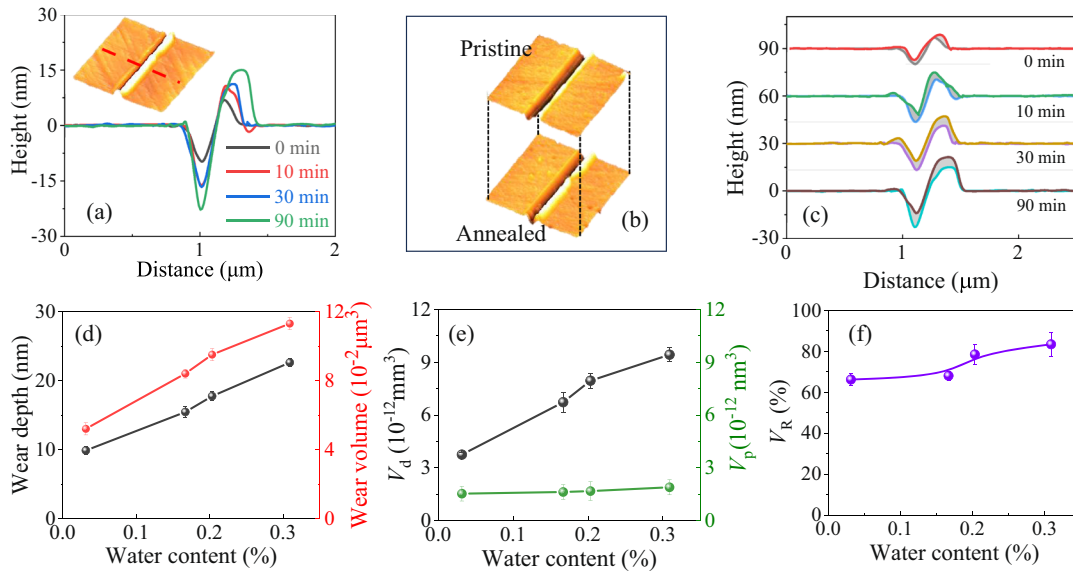


Fig. 6 Nanowear and its subsurface deformation caused by the corrosion. **a** Typical cross-section line profile of nanowear on BAS glass surface under various corrosion conditions. **b** AFM image and **c** cross-section line profile of residual nanowear imprint as well as the corresponding annealed nanowear imprint. **d** Wear depth and volume of nanowear mark obtained from **b** as a function of water content in the AL. **e** Volumes of plastic flow (V_p) and densification (V_d), **f** Volume recovery ratio (V_R) of corroded BAS glass surface as a function of water content in the AL. The error bars in Figs. 6d–f are based on the standard deviation of 6 measurements for each sample.

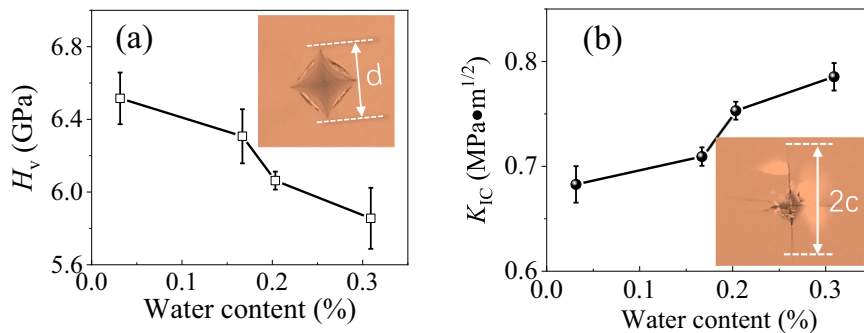


Fig. 7 Mechanical properties of glass surface determined by Vicker indentation. **a** Vickers hardness (H_v) and **b** indentation fracture toughness (K_{IC}) of glass surfaces as a function of water content in AL. The error bars are based on the standard deviation of 23 measurements for each sample.

After the static corrosion tests, the concentrations of leachable alkali and alkaline-earth ions (e.g., sodium, calcium, and magnesium) were measured by the Time-of-flight secondary-ion mass spectroscopy (TOF-SIMS 5-100, ION-TOF GmbH, Germany). The acceleration voltage of the Bi^+ primary ion beam was 30 keV. The scanning area was $50 \times 50 \mu\text{m}^2$ for negative secondary ion detection with an incidence angle of 45° to the sample surface normal. The acceleration voltage of the O^{2+} Sputter ion beam was 1 keV, and the scanning area was $200 \times 200 \mu\text{m}^2$ for negative secondary ion detection with an incidence angle of 45° to the surface normal direction. Chemical structure of corroded glass surface was also analyzed with a confocal micro-Raman spectroscopy (Renishaw In Via, Renishaw, UK) in the range from 400 to 4000 cm^{-1} with a resolution of 2 cm^{-1} .

Sum frequency generation vibration spectroscopy (SFG) was used to detect the hydrogen bonding interaction of adsorbed water molecules on corroded glass surface in various humid environments. During the SFG measurements, visible light ω_{VIS} and infrared light ω_{IR} were adjusted to overlap in space and time, resulting in a sum signal ω_{SFG} , where the signal strength can be expressed as $\omega_{\text{SFG}} = \omega_{\text{VIS}} + \omega_{\text{IR}}$. In the present study, visible pulses

(532 nm) and tunable IR pulses (2.5–10 μm) generated with an EKSPILA laser system were spatially and temporally overlapped at the BAS glass surface. The incident angles of visible and IR pulses were 50° and 55° with respect to the surface normal, respectively. The SFG signal intensity was normalized with the intensities of input visible and IR beams. The polarization combination for the spectra collected was *s* for SFG signal, *s* for visible beam, and *p* for IR beam (*ssp*). The environment temperature was kept at $20 \pm 0.5^\circ \text{C}$, while the relative humidity (RH) for the SFG measurements were set as 50% RH.

Nanoindentation tests were conducted with a Berkovich diamond tip upon a nanomechanical tester (Agilent G200, Keysight, USA). The indentation depth was set to be 300 nm. At least fifteen indentations were made on each glass specimen to obtain accurate statistical values. The measurements were performed in humid air (50% RH) at 23°C . After the nanoindentation tests, the topography of the residual imprint mark on glass surfaces was scanned with a sensitive silicon nitride tip (μ -Masch Technologies, USA) in the tapping mode with an atomic force microscopy system (AFM, SPI3800N, Seiko, Japan). The nominal radius of silicon nitride tip was 8 nm and the nominal spring

constant was 40 N/m. The scan size of all AFM image was $5 \times 5 \mu\text{m}^2$.

All nanowear tests were carried out using an AFM system upon a cubic corner diamond tip with a nominal radius of $\sim 540 \text{ nm}$ (Micro Star Technologies, USA). The spring constants of the tip cantilevers were $\sim 254 \text{ N/m}$. The nanowear tests was made under an applied constant load of $50 \mu\text{N}$ with 400 sliding cycles, and the sliding distance and velocity for each cycle were $4 \mu\text{m}$ and $4 \mu\text{m/s}$, respectively. All nanowear tests were conducted under the relative humidity and room temperature ($\sim 50\% \text{ RH}$, $\sim 23^\circ\text{C}$), and at least five wear tests were conducted under each testing condition to ensure the reliability of the experiments. The topography of nanowear track on glass surfaces was in-situ scanned by a silicon nitride tip ($\mu\text{-Masch}$ Technologies, USA) with a nominal radius of 8 nm and a spring constant of 40 N/m . To study the subsurface deformation mechanism of BAS glass upon nanoscratch and nanoindentation, all the glass samples were annealed at $0.9 \times T_g$ (K) for 2 h, and then the residual imprint and scratch tracks on glass surface were in-situ re-imaged again³¹.

Vickers indentation tests of glass substrates were performed by Vickers hardness tester (HXD-1000TMC/LCD, Shanghai Taiming Optics Co. Ltd, China). The normal load was set as 3 N. More details about the Vickers indentation tests can be found in our previous publication⁴⁵. The Vickers hardness (H_V) could be calculated by^{45–48}:

$$H_V = \frac{1.8544 \times P}{d^2} \quad (1)$$

where d is the diagonal length of the residual imprint indentation under a given applied normal load P . The Vickers indentation fracture toughness (K_{IC}) was measured by:

$$K_{IC} = \varepsilon \left(\frac{E}{H_V} \right) \frac{P}{c_0^{3/2}} \quad (2)$$

where ε is the geometric factor set as 0.016, E is the elastic modulus of glass materials, P is the applied load in N , and c_0 is the length of radial/median cracks measured from the center of the indent impression. The average and standard deviation were obtained from more than 20 measurements for each sample.

DATA AVAILABILITY

The data supporting the main findings are available within the manuscript and supplementary information. Additional supporting data can be obtained from the corresponding authors upon reasonable request.

Received: 14 October 2023; Accepted: 14 January 2024;

Published online: 03 February 2024

REFERENCES

- Ramakanth, D., Singh, S., Maji, P. K., Lee, Y. S. & Gaikwad, K. K.K. Advanced packaging for distribution and storage of COVID-19 vaccines: a review. *Environ. Chem. Lett.* **19**, 3597–3608 (2021).
- Haynes, B. F. et al. Prospects for a safe COVID-19 vaccine. *Sci. Transl. Med.* **12**, 0948 (2020).
- Guadagnino, E., Guglielmi, M. & Nicoletti, F. Glass: The best material for pharmaceutical packaging. *Int. J. Appl. Glass Sci.* **13**, 281–291 (2022).
- Kim, J. H., Marks, F. & Clemens, J. D. Looking beyond COVID-19 vaccine phase 3 trials. *Nat. Med.* **27**, 205–211 (2021).
- Bohrer, D., Bortoluzzi, F., Nascimento, P. C., Carvalho, L. M. & Ramirez, A. G. Silicate release from glass for pharmaceutical preparations. *Int. J. Pharm.* **355**, 174–183 (2008).
- Wondraczek, L. et al. Advancing the mechanical performance of glasses: perspectives and challenges. *Adv. Mater.* **34**, 2109029 (2022).
- Shanley, A. Can pharma quality go high tech? *Pharm. Technol.* **44**, 16–19 (2020).
- Tanaka, H., Tong, H., Shi, R. & Russo, J. Revealing key structural features hidden in liquids and glasses. *Nat. Rev. Phys.* **1**, 333–348 (2019).
- Gin, S., Abdelouas, A. & Criscenti, L. J. An international initiative on long-term behavior of high-level nuclear waste glass. *Mater. Today* **16**, 243–248 (2013).
- Kolluru, P. V., Green, D. J., Pantano, C. G. & Muhlstein, C. L. Effects of surface chemistry on the nanomechanical properties of commercial float glass. *J. Am. Ceram. Soc.* **93**, 838–847 (2010).
- Tadjiev, D. R. & Hand, R. J. Surface hydration and nanoindentation of silicate glasses. *J. Non-Cryst. Solids* **356**, 102–108 (2010).
- Hellmann, R. et al. Nanometre-scale evidence for interfacial dissolution–reprecipitation control of silicate glass corrosion. *Nat. Mater.* **14**, 307–311 (2015).
- Banerjee, J., Bojan, V., Pantano, C. G. & Kim, S. H. Effect of heat treatment on the surface chemical structure of glass: oxygen speciation from in situ XPS analysis. *J. Am. Ceram. Soc.* **101**, 644–656 (2018).
- Sekine, T., Suzuki, T. & Yamamoto, K. Inward migration of glass-modifier cations during heat treatment under an N_2 atmosphere. *J. Am. Ceram. Soc.* **98**, 1464–1470 (2015).
- Natrup, F., Bracht, H., Murugavel, S. & Roling, B. Cation diffusion and ionic conductivity in soda-lime silicate glasses. *Phys. Chem.* **7**, 2279 (2005).
- Gin, S. et al. Origin and consequences of silicate glass passivation by surface layers. *Nat. Commun.* **6**, 6360–7360 (2015).
- Ojovan, M. I., Pankov, A. S. & Lee, W. E. The ion exchange phase in corrosion of nuclear waste glasses. *J. Nucl. Mater.* **358**, 57–68 (2006).
- Thomas, R. Determination of water contents of granite melt inclusions by confocal laser Raman microprobe spectroscopy. *Am. Mineral.* **85**, 868–872 (2000).
- Bonechi, B. et al. Micro-Raman water calibration in ultrapotassic silicate glasses: Application to phono-tephrites and K-fooidites of Colli Albani Volcanic District (Central Italy). *Chem. Geol.* **597**, 120816 (2022).
- Luo, J., Huynh, H., Pantano, C. G. & Kim, S. H. Hydrothermal reactions of soda lime silica glass- revealing subsurface damage and alteration of mechanical properties and chemical structure of glass surfaces. *J. Non-Cryst. Solids* **452**, 93–101 (2016).
- He, H., Luo, J., Qian, L., Pantano, C. G. & Kim, S. H. Thermal Poling of soda- lime silica glass with nonblocking electrodes-Part 2: effects on mechanical and mechanochemical properties. *J. Am. Ceram. Soc.* **99**, 1231–1238 (2016).
- Oliver, W. C. & Pharr, G. M. Measurement of hardness and elastic modulus by instrumented indentation: advances in understanding and refinements to methodology. *J. Mater. Res.* **19**, 3–20 (2004).
- Pharr, G. M. Measurement of mechanical properties by ultra- low load indentation. *Mater. Sci. Eng. A* **253**, 151–159 (1998).
- Qiao, Q., Gu, F., Xiao, T., Yu, J. & He, H. Synergetic effects of water and SO_2 treatments on mechanical and mechanochemical properties of soda lime silicate glass. *J. Non-Cryst. Solids* **562**, 120774 (2021).
- Amma, S., Luo, J., Kim, S. H. & Pantano, C. G. Effect of glass composition on the hardness of surface layers on aluminosilicate glasses formed through reaction with strong acid. *J. Am. Ceram. Soc.* **101**, 657–665 (2018).
- Montenegro, A. et al. Asymmetric response of interfacial water to applied electric fields. *Nature* **594**, 62–65 (2021).
- Li, C. et al. In situ probing electrified interfacial water structures at atomically flat surfaces. *Nat. Mater.* **18**, 697–701 (2019).
- Ciccotti, M. Stress-corrosion mechanisms in silicate glasses. *J. Phys. D: Appl. Phys.* **42**, 214006 (2009).
- Rouxel, T., Jang, J. & Ramamurty, U. Indentation of glasses. *Prog. Mater. Sci.* **121**, 100834 (2021).
- Ji, H., Keryvin, V., Rouxel, T. & Hammouda, T. Densification of window glass under very high pressure and its relevance to Vickers indentation. *Scr. Mater.* **55**, 1159–1162 (2006).
- Yoshida, S., Sangleboeuf, J. & Rouxel, T. Quantitative evaluation of indentation-induced densification in glass. *J. Mater. Res.* **20**, 3404–3412 (2005).
- Rouxel, T., Ji, H., Hammouda, T. & Moréac, A. Poisson's ratio and the densification of glass under high pressure. *Phys. Rev. Lett.* **100**, 225501 (2008).
- Keryvin, V., Charleux, L., Hin, R., Guin, J. P. & Sangleboeuf, J. C. Mechanical behaviour of fully densified silica glass under Vickers indentation. *Acta Mater.* **129**, 492–499 (2017).
- Sellappan, P. et al. Composition dependence of indentation deformation and indentation cracking in glass. *Acta Mater.* **61**, 5949–5965 (2013).
- Sheth, N. et al. Influence of acid leaching surface treatment on indentation cracking of soda lime silicate glass. *J. Non-Cryst. Solids* **543**, 120144 (2020).
- Ogrinc, A. L., Zhou, Y., Hahn, S. H., Lin, Y. & Kim, S. H. Revealing the structure of the sodium-leached layer of soda lime silica glass: A comprehensive spectroscopic analysis. *J. Non-Cryst. Solids* **600**, 121989 (2023).
- Ding, Z. et al. Topological understanding of the mixed alkaline earth effect in glass. *J. Non-Cryst. Solids* **527**, 119696 (2020).
- Ren, M., Deng, L. & Du, J. Bulk, surface structures and properties of sodium borosilicate and boroaluminosilicate nuclear waste glasses from molecular dynamics simulations. *J. Non-Cryst. Solids* **476**, 87–94 (2017).
- Ojovan, M. I. Mass spectrometric evidencing on modified random network microstructure and medium range order in silicate glasses. *J. Non-Cryst. Solids* **434**, 71–78 (2016).

40. Yang, R. et al. Chemical durability of borosilicate pharmaceutical glasses: Mixed alkaline earth effect with varying [MgO]/[CaO] ratio. *J. Am. Ceram. Soc.* **104**, 3973–3981 (2021).
41. Ditter, D. et al. Evaluation of glass delamination risk in pharmaceutical 10 mL/10 R vials. *J. Pharma. Sci.* **107**, 624–637 (2018).
42. Raina, H. & Jindal, A. Packaging of non-injectable liquid pharmaceuticals: A Review. *J. Appl. Pharm. Sci.* **7**, 248–257 (2017).
43. Thorpe, C. L. et al. Forty years of durability assessment of nuclear waste glass by standard methods. *npj Mater. Degrad.* **5**, 61 (2021).
44. Nava-Fariás, L. et al. Applying laboratory methods for durability assessment of vitrified material to archaeological samples. *npj Mater. Degrad.* **5**, 57 (2021).
45. Lai, Y., Gu, F., Yu, J. & He, H. Environment dependence of hardness and fracture toughness of soda lime silica glass in humid and liquid conditions. *J. Non-Cryst. Solids* **569**, 120985 (2021).
46. Hermansen, C. et al. Densification and plastic deformation under microindentation in silicate glasses and the relation to hardness and crack resistance. *J. Non-Cryst. Solids* **364**, 40–43 (2013).
47. Lund, M.D. & Yue, Y.Z., Influences of chemical ageing on the surface morphology and crystallization behavior of basaltic glass fiber. *J. Non-Cryst. Solids* **354**, 1151–1154 (2008).
48. Okhrimenko, D.V., Barly, S.H.Q., Jensen, M., Lakshmanov, L.Z., Johansson, D.B., Solvang, M., Yue, Y.Z. & Stipp, S.L.S., Surface evolution of aluminosilicate glass fibers during dissolution: influence of pH, solid-to-solution ratio and organic treatment. *J. Colloid Interface Sci.* **606**, 1983–1997 (2022).

ACKNOWLEDGEMENTS

The authors are grateful for the financial support from the National Natural Science Foundation of China (Grant No. 52372006, 51975492), Taishan Youth Scholar Project of Shandong Province (Grant No. 202211209), and Major innovation project for integrating science, education & industry of Qilu University of Technology (Shandong Academy of Sciences) (Grant No. 2022JBZ01-07).

AUTHOR CONTRIBUTIONS

Q.Z., Y.Y., and H.H. conceived the project. Q.Z. processed the sample in the laboratory. X.M. processed and interpreted the ToF-SIMS and ICP data. Y.M. performed the SFG experiments and interpreted the data. H.H. performed the Vickers indentation,

nanindentation, and nanowear tests. Q.Z. and H.H. prepared the manuscript draft. J.Y. and Y.Y. participated in valuable discussions and provided useful feedback during manuscript preparation. All authors contributed to reviewing the final manuscript.

COMPETING INTERESTS

The authors declare no competing interests.

ADDITIONAL INFORMATION

Supplementary information The online version contains supplementary material available at <https://doi.org/10.1038/s41529-024-00431-3>.

Correspondence and requests for materials should be addressed to Yuanzheng Yue or Hongtu He.

Reprints and permission information is available at <http://www.nature.com/reprints>

Publisher's note Springer Nature remains neutral with regard to jurisdictional claims in published maps and institutional affiliations.



Open Access This article is licensed under a Creative Commons Attribution 4.0 International License, which permits use, sharing, adaptation, distribution and reproduction in any medium or format, as long as you give appropriate credit to the original author(s) and the source, provide a link to the Creative Commons license, and indicate if changes were made. The images or other third party material in this article are included in the article's Creative Commons license, unless indicated otherwise in a credit line to the material. If material is not included in the article's Creative Commons license and your intended use is not permitted by statutory regulation or exceeds the permitted use, you will need to obtain permission directly from the copyright holder. To view a copy of this license, visit <http://creativecommons.org/licenses/by/4.0/>.

© The Author(s) 2024